PHYSICAL REVIEW C **109**, 064609 (2024)

Universal separable structure of the optical potential

H. F. Arellano[1,2] and G. Blanchon[2,3]
[1]*Department of Physics-FCFM, University of Chile, Av. Blanco Encalada 2008, RM 8370449 Santiago, Chile*
[2]*CEA, DAM, DIF, F-91297 Arpajon, France*
[3]*Université Paris-Saclay, CEA, LMCE, 91680 Bruyíres-le-Châtel, France*

(Received 28 February 2024; revised 12 May 2024; accepted 21 May 2024; published 10 June 2024)

Based on a momentum-space *in-medium* folding model, we disclose the universal separability of the optical potential, revealing its radial and nonlocality features at beam energies in the range 40–400 MeV and target mass numbers in the range $40 \leqslant A \leqslant 208$. From this microscopic study we find that the nonlocality form factor is inherently complex and of hydrogenic nature, affecting both central and spin-orbit components of the potential. A striking outcome from this study is the consistent appearance of a nodal point in the imaginary radial form factor, notably suppressing surface absorption peaks, in evident contrast with Woods-Saxon's assumption of an absorptive peak at the nuclear surface. Our analysis reveals that the complex radial form factor can effectively be represented as convolutions of uniform spherical distribution with a Gaussian form factor and a Yukawa term. These robust microscopically driven findings offer new ways for investigating nuclear reactions beyond the restricting Woods-Saxon and Perey-Buck assumptions.

DOI: 10.1103/PhysRevC.109.064609

I. INTRODUCTION

Supernovae, nuclear spallation, stockpile stewardship, neutron star mergers, nuclear reactors, among many others, constitute scenarios where multiple nuclear reactions involving stable and exotic nuclei take place. In this context the optical potential emerges as a primary tool to quantify scattering and reaction processes [1]. Along this line, phenomenological approaches inspired by Woods-Saxon form factors [2], supplemented with Perey-Buck nonlocal form factor [3], have been developed with reasonable success [3–6]. Despite these advances, there is no theoretical justification for the prescribed form factors associated to flux absorption nor the nonlocality, a situation which may hinder global models from further improvements.

From a fundamental standpoint, the challenge is to describe nucleon-nucleus (*NA*) scattering starting from the basic internucleon interaction. A final and ambitious goal would be to be able to describe scattering processes over a broad energy range—from a few keV up to hundreds of MeV—and considering targets over the whole nuclear chart. To this end we rely on *ab initio* approaches [7–10] and *in-medium* microscopic models [11,12]. Despite the significant advances reported in the context of *ab initio* approaches, current applications are limited to few light targets and low energies, reaching qualitative agreement with the data. Microscopic models, on the other hand, constitute a reasonable and flexible framework to bridge the basic nucleon-nucleon (*NN*) interaction with the optical potential by means of density-dependent *NN* effective interactions.

Following a previous work, where a bell-shape nonlocality in the optical potential was first disclosed [13], we further scrutinize its momentum-space structure to extract its radial as well as nonlocal form factors. The study we report here is based on the Argonne v_{18}*NN* potential (AV18) [14], suited for *NA* scattering at the energies considered, provided minimal relativity is accounted for [15]. In this case the *in medium* effective interaction is taken from the genuine fully off-shell g matrix solutions of the Brueckner-Hartree-Fock integral equation. Emphasis is given to retain the genuine nonlocality of the optical potential at all stages of its calculation.

This work is organized as follows. In Sec. I we introduce the general framework of the microscopic model, followed by Sec. III where we present and discuss the separability of the optical potential from actual folding calculations. In Sec. IV we present final remarks.

II. FRAMEWORK

The nonrelativistic optical-model potential in momentum space for nucleon elastic scattering off spin-zero nucleus can be expressed as [16]

$$\tilde{\mathcal{U}}(\boldsymbol{k}',\boldsymbol{k};E) = \tilde{\mathcal{U}}_c(\boldsymbol{k}',\boldsymbol{k};E) + i\boldsymbol{\sigma}\cdot\hat{\boldsymbol{n}}\,\tilde{\mathcal{U}}_{so}(\boldsymbol{k}',\boldsymbol{k};E) \qquad (1)$$

with E the center-of-mass (c.m.) kinetic energy, $\frac{1}{2}\boldsymbol{\sigma}$ the spin of the projectile, and $\hat{\boldsymbol{n}}$ a unit vector perpendicular to the scattering plane given by $\hat{\boldsymbol{n}} = \boldsymbol{k}'\times\boldsymbol{k}/|\boldsymbol{k}'\times\boldsymbol{k}|$. Here, $\tilde{\mathcal{U}}_c$ and $\tilde{\mathcal{U}}_{so}$ denote the central and spin-orbit components of the potential expressed in terms of the relative momenta $\boldsymbol{k}$ and $\boldsymbol{k}'$. To calculate the potential we follow Refs. [11,15,17], based on an infinite nuclear-matter model to represent the *in-medium* *NN* effective interaction starting from realistic *NN* bare potentials [18]. The use of the Slater approximation [11,19] for the one-body mixed density yields the simplified

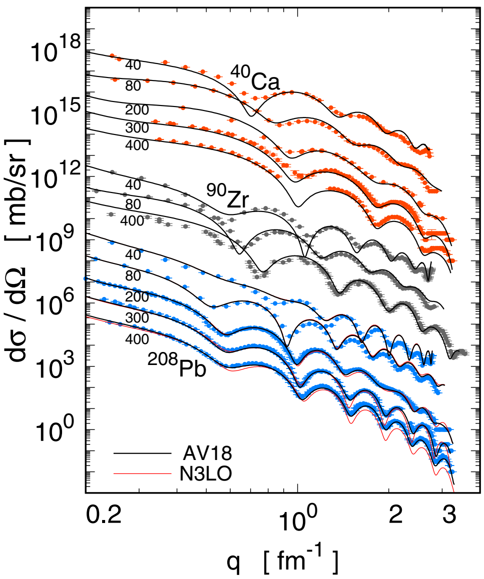

FIG. 1. Differential cross section for proton-nucleus elastic scattering as function of the momentum transfer based on AV18 (black curves) and N3LO (red curves) bare potentials. The data are taken from Refs. [23–26].

form

$$\tilde{\mathcal{U}}(\boldsymbol{k}',\boldsymbol{k};E) = 4\pi \sum_{\alpha=p,n} \int_0^\infty z^2 dz\, \rho_\alpha(z) j_0(qz) \times \int d\boldsymbol{P}\, n_z(P) \left\langle \frac{1}{2}(\boldsymbol{k}'-\boldsymbol{P}) \middle| g^{p\alpha}_{\bar{K}}(E+\bar{\epsilon}) \middle| \frac{1}{2}(\boldsymbol{k}-\boldsymbol{P}) \right\rangle_{\mathcal{A}} \tag{2}$$

with $\mathcal{A}$ denoting antisymmetrization and $\rho_\alpha(z)$ the density of nuclear species α at coordinate z. Additionally, the g matrix is evaluated at the isoscalar density $\rho(z)$, coupling the projectile p with target nucleon α. In the above $n_z(P)$ sets bounds for the off-shell contributions in the g matrix at coordinate z.

Calculations of optical potentials as in Eq. (2) rely on two main inputs: proton and neutron ground-state densities, which in this work are taken from Hartree-Fock calculations of Ref. [20]; and the bare *NN* potential, which we have chosen AV18 because of its ability to account for *NN* scattering data up to 320 MeV. This bare interaction is used to calculate *NN* g matrices fully off-shell over a mesh of Fermi momenta k_F. We refer the reader to Ref. [18] for further details. The scattering observables for the resulting nonlocal optical potentials in momentum space are calculated using the SWANLOP package [21], based on Ref. [22], treating nonlocalities in the presence of the Coulomb interaction without approximations.

The consistency between the microscopic model and available data is illustrated in Fig. 1, where we plot the measured [23–26] and calculated [21] differential cross sections for proton-nucleus scattering as functions of the momentum transfer. The targets are ^{40}Ca, ^{90}Zr and ^{208}Pb, at the beam energies of 40, 80, 200, 300, and 400 MeV. Black curves denote results based on AV18. Being aware that chiral potentials are not suited for high energies, we still find instructive to illustrate its behavior at energies of this study. Thus, we consider the chiral *NN* potential up to next-to-next-to-next-to-leading order (N3LO) [27]. Results for $p+{}^{208}$Pb scattering based on this chiral interaction are shown with red curves. As observed, the folding model based on AV18 yields a reasonable description of the scattering data. In the case of 40 MeV the calculated differential cross section appears slightly more diffractive than the data, leading us to set this as the lowest energy for our study. In the case of the N3LO interaction for $p+{}^{208}$Pb we observe a gradual departure of its results from the data, an indication of upper energy limit of about 290 MeV for this bare interaction.

III. SEPARABILITY

The optical potential in Eq. (2), expressed in terms of relative momenta $\boldsymbol{k}$ and $\boldsymbol{k}'$, can be reexpressed in terms of the momentum transfer $\boldsymbol{q}$ and the mean momentum $\boldsymbol{K}$, namely,

$$\boldsymbol{K} = \tfrac{1}{2}(\boldsymbol{k}+\boldsymbol{k}'), \tag{3a}$$

$$\boldsymbol{q} = \boldsymbol{k}-\boldsymbol{k}'. \tag{3b}$$

Hence, if we denote $\tilde{U}(\boldsymbol{K},\boldsymbol{q}) = \tilde{\mathcal{U}}(\boldsymbol{k}',\boldsymbol{k};E)$, then

$$\tilde{U}(\boldsymbol{K},\boldsymbol{q}) = \tilde{U}_c(\boldsymbol{K},\boldsymbol{q}) + i\boldsymbol{\sigma}\cdot(\boldsymbol{K}\times\boldsymbol{q})\,\tilde{U}_{so}(\boldsymbol{K},\boldsymbol{q}). \tag{4}$$

Each component, $\tilde{U}_c$ and $\tilde{U}_{so}$, can then be expanded in terms of Legendre polynomials of $w=\hat{\boldsymbol{K}}\cdot\hat{\boldsymbol{q}}$. In this way we express $\tilde{U}_c(\boldsymbol{K},\boldsymbol{q}) = \sum_{n=0}^{\infty} \tilde{U}_n^{(c)}(K,q) P_n(w)$, together with $|\boldsymbol{K}\times\boldsymbol{q}|\tilde{U}_{so}(\boldsymbol{K},\boldsymbol{q}) = Kq\sum_{n=0}^{\infty} \tilde{U}_{n+1}^{(so)}(K,q) P_{n+1}^1(w)$. In a recent study [28] we found that the zeroth-order contribution in each expansion is sufficient to accurately describe the scattering observables of the original potential. This remarkable property validates focusing solely on the $n=0$ terms, justifying the notation $\tilde{U}_c(\boldsymbol{K},\boldsymbol{q}) \to \tilde{U}_c(K,q)$, and $\tilde{U}_{so}(\boldsymbol{K},\boldsymbol{q}) \to \tilde{U}_{so}(K,q)$.

To isolate the nonlocality of $\tilde{U}_c(K,q)$ and $\tilde{U}_{so}(K,q)$, for now denoted as $\tilde{U}(K,q)$, we define $J/(2\pi)^3 = \tilde{U}(0,0)$, together with the ratios

$$\tilde{V}(K,q) = \frac{\tilde{U}(K,q)}{\tilde{U}(K,0)}, \tag{5a}$$

$$\tilde{H}(K) = \frac{\tilde{U}(K,0)}{\tilde{U}(0,0)}. \tag{5b}$$

Note that $\tilde{V}(K,q)$ and $\tilde{H}(K)$ are complex and dimensionless, satisfying $\tilde{V}(K,0) = \tilde{H}(0) = 1$. Additionally, J is also complex, representing the volume integral of the potential. With these definitions $\tilde{U}(K,q)$ factorizes as

$$\tilde{U}(K,q) = \frac{J}{(2\pi)^3}\,\tilde{V}(K,q)\,\tilde{H}(K). \tag{6}$$

In Ref. [13] it was noted that $\tilde{V}(K,q)$ has a weak dependence on K. We have examined this dependency and found that by setting $\tilde{V}(K,q) = \tilde{V}(k_0,q)$, with k_0 the on-shell momentum in the c.m. reference frame, the factorization in Eq. (6) reproduces the scattering observables of the original potential. By making this choice we ensure that the forward $(q=0)$ on-shell matrix element of the potential is reproduced. This result motivates the definition of the radial form factor, $\tilde{v}(q) = \tilde{V}(k_0,q)$. The denomination *radial* refers to the

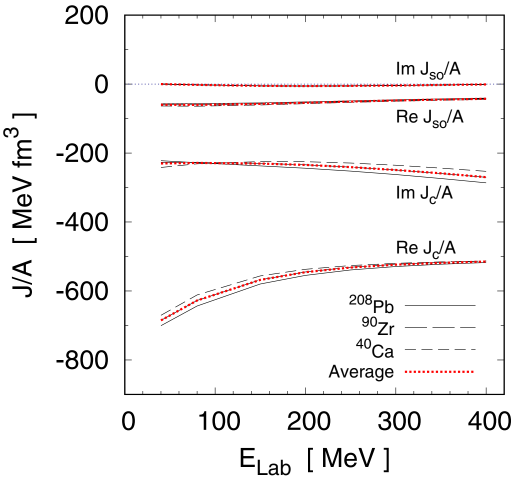

FIG. 2. Volume integrals per nucleon J_c/A and J_{so}/A as functions of the beam energy.

fact that the conjugate coordinate of q corresponds to the mean radial distance between the projectile and the center of the target, hereafter denoted as r. The above considerations lead to

$$\tilde{U}(K,q) = \frac{J}{(2\pi)^3}\,\tilde{v}(q)\,\tilde{H}(K), \tag{7}$$

to be referred as *JvH* factorization. We now examine each of its three terms.

A. The volume integral *J*

In momentum space, the volume integral J of the potential is obtained from its matrix element at $\boldsymbol{k}=\boldsymbol{k}'=0$, that is to say $\tilde{U}(0,0)$. In Fig. 2 we plot the volume integrals of the potential over the number of target nucleons, J/A, as function of the beam energy. In the following, subscripts c and so denote central and spin-orbit components, respectively. Solid, long-dashed and dashed curves denote results for ^{208}Pb, ^{90}Zr, and ^{40}Ca, respectively. As observed, Re $[J_c/A]$ is the strongest term, decreasing monotonically its magnitude by about 25% over the range 40–400 MeV. The imaginary term, on the other hand, is much weaker but increasing its magnitude by ∼17% over the same energy range. The spin-orbit strengths J_{so}/A are nearly real and constant, amounting to less than 10% of Re $[J_c/A]$. We have verified that the averaged J_c/A and J_{so}/A, considering all three targets and evaluated at each beam energy, yield nearly the same scattering observables as the ones obtained from the original potential. These averages are shown with dotted red curves.

B. The radial form factor *v*

We now examine the central $\tilde{v}_c(q)=\tilde{V}_c(k_0,q)$ and spin-orbit $\tilde{v}_{so}(q)=\tilde{V}_{so}(k_0,q)$ form factors. In panels (a) and (b) of Fig. 3 we show the central $\tilde{v}_c$ and spin-orbit $\tilde{v}_{so}$ radial potentials as functions of q, respectively. These correspond to microscopic calculations for $p+{}^{40}$Ca elastic scattering at 40, 80, 200, 300, and 400 MeV shown with dotted, short-dashed, dashed, long-dashed, and solid curves, respectively. The insets show logarithmic plots for |Re $\tilde{v}_c$| and |Re $\tilde{v}_{so}$| (black curves), and the ratios |Im $\tilde{v}_c/q^2$| and |Im $\tilde{v}_{so}/q^2$| (red curves). Blue solid curves correspond to $\tilde{\rho}_{SL}(qR) = 3\,j_1(qR)/qR$, the Slater density to be discussed later.

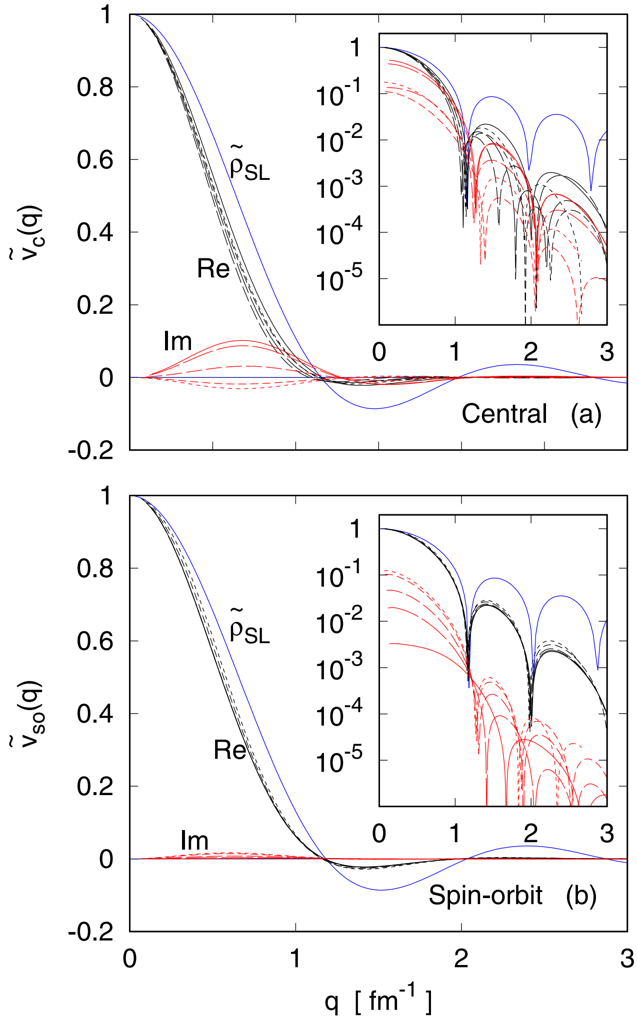

FIG. 3. Central (a) and spin-orbit (b) radial form factors as functions of the momentum transfer in the case of $p+{}^{40}$Ca scattering. Results at 40, 80, 200, 300, and 400 MeV are shown with dotted, short-dashed, dashed, long-dashed, and solid curves, respectively. Blue solid curves represent $\tilde{\rho}_{SL}(qR)$ (see text). Red curves in the insets represent $|\mathrm{Im}\,\tilde{v}(q)|/q^2$.

We observe similar diffractive patterns for the real components of $\tilde{v}_c$ in panel (a) and $\tilde{v}_{so}$ in panel (b) with their first nodes at $q\approx 1$ and 1.1 fm^{-1}, respectively. In the case of their imaginary components we found that they behave as $\sim q^2$ near the origin, feature displayed in both insets, where red curves represent Im $[\tilde{v}(q)/q^2]$. As observed, the diffractive pattern of this ratio is qualitatively similar to that of their real counterparts. Apart from the exact location of the nodes, the diffractive behavior of the Slater density $\rho_{SL}(qR)$ has an appealing resemblance with those shown with black and red curves in the insets. This observation becomes useful for the upcoming discussion.

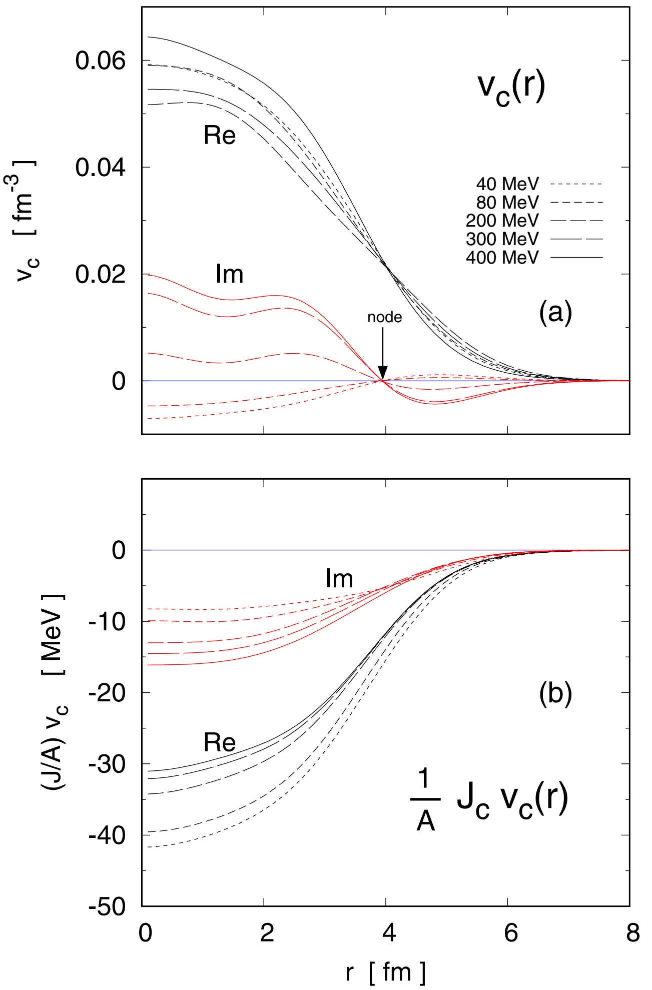

FIG. 4. Coordinate-space radial form factor $v_c(r)$ (a) and product $(J/A)v_c(r)$ (b) as functions of r. Curve patterns follow the same convention as in Fig. 3.

The radial form factors in coordinate space for the central potential, $v_c(r)$, are displayed in panel (a) of Fig. 4. These correspond to $p+{}^{40}$Ca scattering at the same energies considered in Fig. 3, for which we adopt the same notation. We note that all Re $[v_c(r)]$ resemble roughly a two-parameter Fermi distribution (2pF). Interestingly, the imaginary part of $v_c(r)$ shows nodal points at nearly the same radius, $r \sim 4$ fm. These nodes are in correspondence with the change of sign in the curvature of Re $[v_c(r)]$, driven by its second derivative. An interpretation of this feature emerges from the q behavior of Im $[\tilde{v}_c(q)/q^2]$ displayed with red curves in the insets of Fig. 3, being qualitatively similar to those for Re $[\tilde{v}_c(q)]$. Thus, q^2 Im $[\tilde{v}_c(q)/q^2]$ would account for nodes near the surface of the 2pF distribution. These peculiar features for v_c are also observed for v_{so}.

The full potential in the JvH form involves the product of three complex terms. The radial part of the optical potential is driven by Jv, the product of the volume integral and the radial form factor, being the natural counterpart of conventional Woods-Saxon potentials. Therefore, if $J = J_r + iJ_i$, and $v = v_r + iv_i$, then the real part of Jv involves a combination of both real and imaginary parts of the radial form factor. The same holds for Im $[Jv]$. With this in mind, features of the radial form factor v differ from those of Jv, the radial potential.

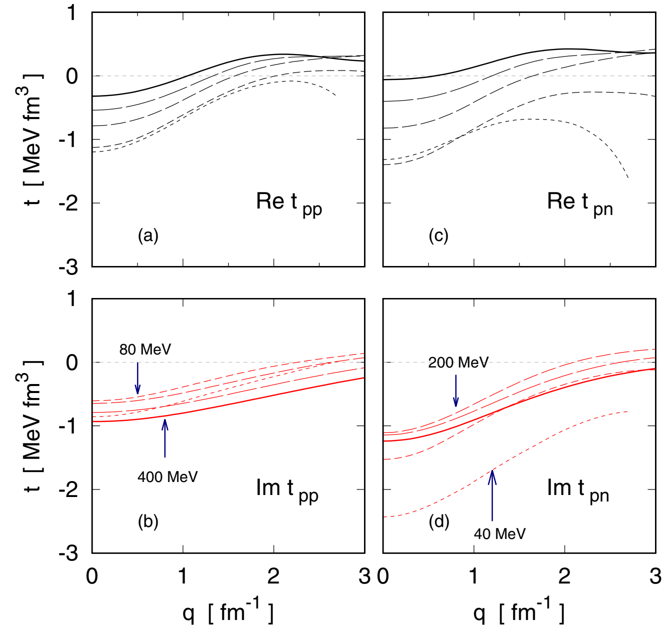

FIG. 5. On-shell t matrix for pp and pn channels as functions of the momentum transfer. Dotted, short-dashed, dashed, long-dashed, and solid curves correspond to 40, 80, 200, 300, and 400 MeV, respectively. Black and red curves correspond to real and imaginary components, respectively.

In panel (b) of Fig. 4 we plot the product $(J/A)v_c$ as function of the radius. As observed, the potential is attractive over the whole range, vanishing smoothly for increasing radius. Even though the imaginary part of $(J/A)v_c$ also vanishes for increasing radius, at 40 MeV the absorption becomes stronger above the surface ($r \gtrsim 4.2$ fm) than that for higher energies. Interestingly, Im $[Jv_c]$ shows no peak at the surface, in contrast with the commonly used Woods-Saxon's prescription to model nuclear absorption phenomenologically. These features for the absorption are also observed for the ^{90}Zr and ^{208}Pb targets.

Going back to panel (a) in Fig. 4 we notice that the maxima of Re v_c, taking place at $r = 0$, is not a monotonic function of the energy. They decrease from 40 MeV up to 200 MeV, followed by a sudden increase evidenced at 400 MeV. This trend is consistent with $\tilde{v}_c(q)$ shown in panel (a) of Fig. 3, with the 400 MeV case (solid curves) above all the other curves. We have investigated the origin of this trend and found that it stems from the behavior of the effective interaction at different energies. To illustrate the point, we have considered the zero-density g matrix in Eq. (2), corresponding to the free t matrix. In this case we examine the on-shell element

$$t_{pp,pn}(q) = \left\langle \tfrac{1}{2}\boldsymbol{k}' \middle| g_{\bar{K}}^{pp,pn}(E) \middle| \tfrac{1}{2}\boldsymbol{k} \right\rangle_{\mathcal{A}}, \tag{8}$$

where $\boldsymbol{q} = \boldsymbol{k} - \boldsymbol{k}'$ with $k = k'$, chosen on-shell in the NA c.m. In Fig. 5 we show the t matrix as function of the momentum transfer q for the pp channel [panels (a) and (b)] and pn

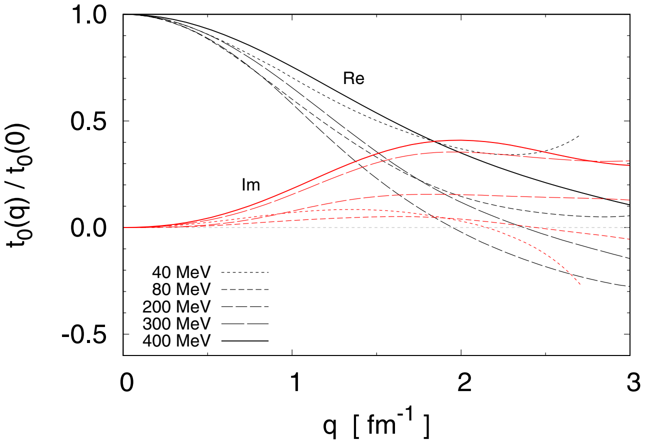

FIG. 6. The isoscalar ratio $t_0(q)/t_0(0)$ as function of the momentum transfer at the same energies as in Fig. 5. Dotted, short-dashed, dashed, long-dashed, and solid curves correspond to 40, 80, 200, 300, and 400 MeV, respectively. Black and red curves denote real and imaginary components, respectively.

channel [panels (c) and (d)]. The upper and lower panels show results for the real and imaginary components, respectively. We observe that the real parts of t follow a smooth behavior as functions of q with clear separation among the curves as the energy increases. Such is not the case for the imaginary components, where the upper and lower curves follow no uniform order, as indicated by the arrows in panels (b) and (d).

Having in mind the "$t\rho$" approximation for the optical potential [16] together with Eq. (5a) for $\tilde{V}(K,q)$, we observe that the radial form factor $\tilde{v}_c(q)$ is closely related to the ratio $t(q)/t(q{=}0)$. Thus, we have calculated this ratio for the isoscalar channel, where $t_0{=}t_{pp}{+}t_{pn}$. In Fig. 6 we plot $t_0(q)/t_0(0)$ at the same energies considered in Fig. 5. It is interesting to note how the curve for 400 MeV stays above the rest, in similar fashion as that for $\tilde{v}_c(q)$ in Fig. 3. This explains why $v_c(0)$ is maximum in the case of 400 MeV, in addition to providing arguments for the nonmonotonicity of the maxima in $v_c(r)$.

C. The nonlocality form factor *H*

In Fig. 7 we plot the resulting nonlocality form factors $\tilde{H}_c$ and H_{so} as functions of K, associated to proton-nucleus scattering at 200 MeV. The targets are ^{208}Pb, ^{90}Zr, and ^{40}Ca, following the same pattern convention as in Fig. 2. The green-shaded profile corresponds to Perey-Buck's nonlocality form factor given by

$$\tilde{H}_{PB} = \exp(-\beta^2K^2/4) \tag{9}$$

with $\beta{=}0.85$ fm, a typical value. We observe that all targets show very similar nonlocal behavior, featuring a weaker decay relative to the Gaussian nonlocality.

Aiming to obtain a simple and accurate representation for $\tilde{H}$, we have found useful to represent it as

$$\tilde{H}(K) = \frac{1}{[1+\eta(K)]^2}\,\frac{1+i\alpha(K)}{1-i\alpha(K)} \tag{10}$$

with η and α real functions obtained directly from $\tilde{H}$.

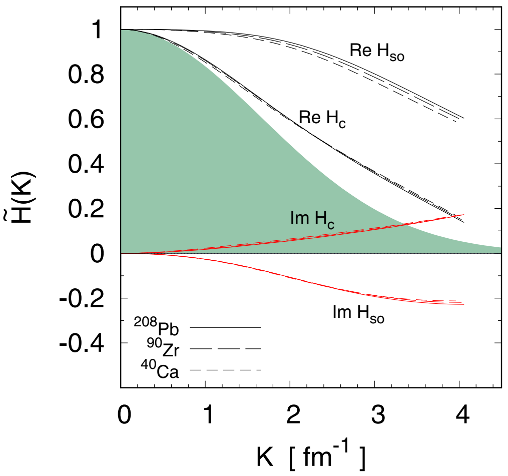

FIG. 7. Bell-shape nonlocality form factor $\tilde{H}(K)$ for *NA* scattering at 200 MeV. The shaded area denotes Perey-Buck nonlocality form factor with $\beta{=}0.84$ fm.

In Fig. 8 we plot the resulting central and spin-orbit η and α as functions of $(K/k_0)^2$ with k_0 the relative momentum in the c.m. reference frame. Numerical labels on each graph denote beam energy in units of MeV. Each bunch of colored curves include results for each of the three targets. We observe that, at a given energy, all three targets yield similar behavior in their respective η and α. Thus, to each of these sets we give

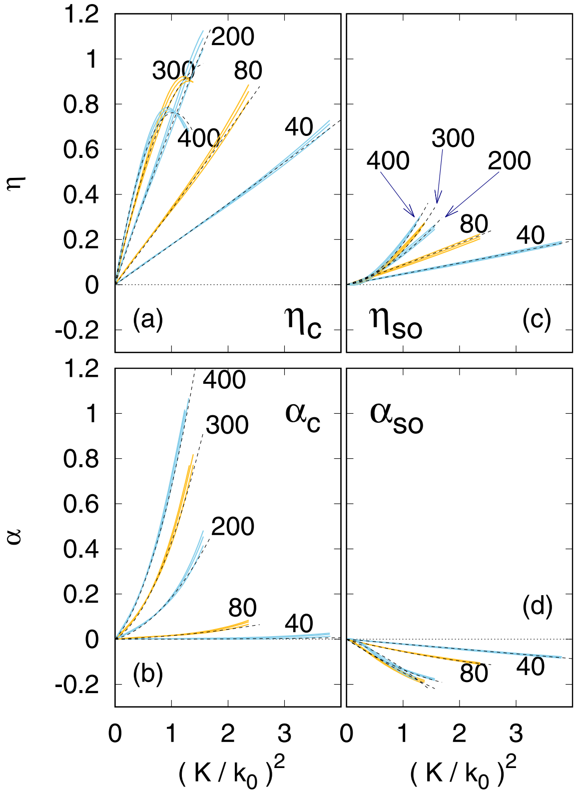

FIG. 8. Nonlocality parameters η and α as functions of $(K/k_0)^2$. See text for explanation of curve patterns.

an optimal quadratic form of the type $(b_1 x + b_2 x^2)$ with $x = (K/k_0)^2$. The resulting parametrizations are shown with dotted curves in Fig. 8, reproducing the scattering observables of the original potential.

The coordinate-space nonlocality form factor is obtained from

$$H(s) = \frac{1}{2\pi^2} \int_0^\infty K^2 dK\, j_0(Ks) \tilde{H}(K) \tag{11}$$

with $s = |\boldsymbol{r}' - \boldsymbol{r}|$ the difference between post and prior NA relative coordinates in Perey-Buck's notation [3]. To gain some insight from Eq. (10) for H we consider the lowest order term in the expansions for η and α. Hence, by expressing $\eta \approx b^2 K^2$, and $\alpha \approx a^2 K^2$, contour integration in the complex plane yields the closed form

$$H(s) = \frac{\left(a^4 + b^4 + 4i\frac{a^2 b^3}{s}\right) e^{-s/b} - 4i\frac{a^2 b^3}{s} e^{-s\sqrt{i}/a}}{8\pi b^3 (b^2 + ia^2)^2}. \tag{12}$$

The real-argument exponential $e^{-s/b}$ accounts for nonlocality of the hydrogenic type of range b, in contrast with the commonly used Gaussian form factor introduced by Perey and Buck. The complex-argument exponential, on the other hand, expresses a strongly dumped oscillatory contribution of range $a\sqrt{2}$. We also note that the nonlocality H is finite at the origin, and that for vanishing a it becomes

$$H(s) = \frac{e^{-s/b}}{8\pi b^3}. \tag{13}$$

D. Global representation

In the preceding sections we have examined the leading features exhibited by each of the three terms participating in the JvH structure of the optical potential. In this section we explore a possible representation of the radial form factors, v_c and v_{so}, retaining the microscopic J/A and nonlocality $\tilde{H}(K)$ expressed by Eq. (10). The aim here is to reproduce as closely as possible the microscopic radial form factors v and with that—through the JvH separable structure of the potential—the scattering observables of the original folding potential.

To obtain a suitable representation for the microscopic $\tilde{v}_c$ and $\tilde{v}_{so}$, we find it useful to consider the Slater density $\tilde{\rho}_{SL}(qR)$, the three-dimensional Fourier transform of a uniform sphere of radius R. The behavior of $\tilde{\rho}_{SL}$ is shown in Fig. 3 with blue curves, with R calibrated to match the first zero of the spherical Bessel function j_1. Although there is no full correspondence between the zeros of $\tilde{v}(q)$ and $\tilde{\rho}_{SL}(qR)$, we have found that by folding additional form factors it is possible to reasonably reproduce the scattering observables of the original microscopic potential. Thus, we have explored the following convolutions:

$$\mathrm{Re}\,[\tilde{v}_{c,so}(q)] = \tilde{\rho}_{SL}(qR_x)\, e^{-a_x^2 q^2}\, \frac{1}{1 + b_x^2 q^2}, \tag{14a}$$

$$\mathrm{Im}\,[\tilde{v}_{c,so}(q)] = c_y\, q^2 \tilde{\rho}_{SL}(qR_y)\, e^{-a_y^2 q^2}\, \frac{1}{1 + b_y^2 q^2}. \tag{14b}$$

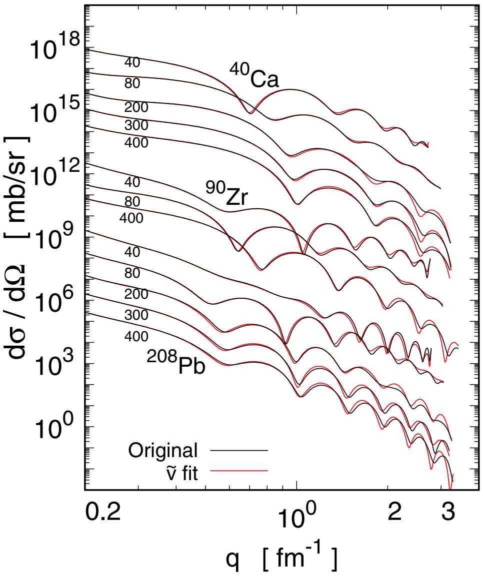

FIG. 9. Differential cross sections as functions of the momentum transfer based on the microscopic folding model (black curves) and global fit for $\tilde{v}(q)$ (red curves).

This construction can be interpreted as if $\tilde{v}_{c,so}$ results from the convolution of a Gaussian-smoothed uniform sphere with a Gaussian-dressed one-meson-exchange interaction. The product of the two Gaussian form factors, also Gaussian, would then account for both the smoothing and the dressing.

We have performed a search of parameters $R_{x,y}$, $a_{x,y}$, $b_{x,y}$, and c_y, for the central and spin-orbit components, to globally reproduce the microscopic $\tilde{v}$ at the five beam energies and the three targets considered in this study. The ability of these global convolutions to reproduce scattering observables of the original microscopic potential is illustrated in Fig. 9, showing with red curves the resulting $d\sigma/d\Omega$ and black curves the ones from the original potential. Although red and black curves do not fully overlap, we note a close correspondence between them. Improvements can be envisaged if separate analyses are made to the coupling to target protons and neutrons, in addition to alternative form factors and search strategies.

IV. CONCLUDING REMARKS

The universal separability of the optical potential is grounded in two elements. The first one is its general form, expressed as $\tilde{\mathcal{U}}(\boldsymbol{k}', \boldsymbol{k}) = \iint d\boldsymbol{p}' d\boldsymbol{p}\, \tilde{\rho}(\boldsymbol{p}', \boldsymbol{p}) \langle \boldsymbol{k}'\boldsymbol{p}' \,|\, T \,|\, \boldsymbol{k}\boldsymbol{p} \rangle_{\mathcal{A}}$, representing the convolution between the off-shell mixed density and a two-body interaction. This general structure is shared by various formulations of the optical-model potential [1,29–32]. In Ref. [33] it was demonstrated that this general expression embodies a well-defined functional structure in terms of the radial coordinate z, characterized by the local density $\rho(z)$, leading to the expression in Eq. (2). The second element lies in the momentum-space structure of the potential, displaying negligible angular dependence when expressed in terms of momenta $\boldsymbol{K}$ and $\boldsymbol{q}$, together with the weak dependence of $\tilde{V}(K, q)$ on K. The emerging complex nonlocality of hydrogenic type, in conjunction with the radial form factors constitute intrinsic and well identifiable components of the microscopic potential. These robust microscopically driven findings offer new ways to investigate nuclear reactions beyond Woods-Saxon and Perey-Buck phenomenological prescriptions. This is particularly relevant for current efforts aimed for the study and description of nuclear reactions for the rare-isotope era [1].

ACKNOWLEDGMENTS

H.F.A. acknowledges partial support provided by the supercomputing infrastructure of the NLHPC (ECM-02): Powered@NLHPC. He also thanks the hospitality of colleagues of CEA-DAM at Bruyères-le-Châtel, where part of this work was done.

[1] C. Hebborn, F. M. Nunes, G. Potel, W. H. Dickhoff, J. W. Holt, M. C. Atkinson, R. B. Baker, C. Barbieri, G. Blanchon, M. Burrows, R. Capote, P. Danielewicz, M. Dupuis, Ch. Elster, J. E. Escher, L. Hlophe, A. Idini, H. Jayatissa, B. P. Kay, K. Kravvaris, J. J. Manfredi, A. Mercenne, B. Morillon, G. Perdikakis, C. D. Pruitt, G. H. Sargsyan, I. J. Thompson, M. Vorabbi, and T. R. Whitehead, Optical potentials for the rare-isotope beam era, J. Phys. G: Nucl. Part. Phys. **50**, 060501 (2023).

[2] R. D. Woods and D. S. Saxon, Diffuse surface optical model for nucleon-nuclei scattering, Phys. Rev. **95**, 577 (1954).

[3] F. Perey and B. Buck, A non-local potential model for the scattering of neutrons by nuclei, Nucl. Phys. **32**, 353 (1962).

[4] A. J. Koning and J. P. Delaroche, Local and global nucleon optical models from 1 keV to 200 MeV, Nucl. Phys. A **713**, 231 (2003).

[5] B. Morillon and P. Romain, Bound single-particle states and scattering of nucleons on spherical nuclei with a global optical model, Phys. Rev. C **76**, 044601 (2007).

[6] Y. Tian, D.-Y. Pang, and Z.-Y. Ma, Systematic nonlocal optical model potential for nucleons, Int. J. Mod. Phys. E **24**, 1550006 (2015).

[7] G. Hagen and N. Michel, Elastic proton scattering of medium mass nuclei from coupled-cluster theory, Phys. Rev. C **86**, 021602(R) (2012).

[8] J. Rotureau, P. Danielewicz, G. Hagen, F. M. Nunes, and T. Papenbrock, Optical potential from first principles, Phys. Rev. C **95**, 024315 (2017).

[9] A. Idini, C. Barbieri, and P. Navrátil, *Ab initio* optical potentials and nucleon scattering on medium mass nuclei, Phys. Rev. Lett. **123**, 092501 (2019).

[10] J. Rotureau, Coupled-cluster computations of optical potential for medium-mass nuclei, Front. Phys. **8**, 285 (2020).

[11] H. F. Arellano, F. A. Brieva, and W. G. Love, In-medium full-folding optical model for nucleon-nucleus elastic scattering, Phys. Rev. C **52**, 301 (1995).

[12] K. Amos, P. J. Dortmans, H. V. von Geramb, S. Karataglidis, and J. Raynal, *Advances in Nuclear Physics*, Vol. 25 of advances in nuclear physics (Springer, New York, 2000).

[13] H. F. Arellano and G. Blanchon, On the separability of microscopic optical model potentials and emerging bell-shape Perey-Buck nonlocality, Eur. Phys. J. A **58**, 119 (2022).

[14] R. B. Wiringa, V. G. J. Stoks, and R. Schiavilla, Accurate nucleon-nucleon potential with charge-independence breaking, Phys. Rev. C **51**, 38 (1995).

[15] H. F. Arellano and H. V. von Geramb, Extension of the full-folding optical model for nucleon-nucleus scattering with applications up to 1.5 GeV, Phys. Rev. C **66**, 024602 (2002).

[16] L. Ray, G. W. Hoffmann, and W. R. Coker, Nonrelativistic and relativistic descriptions of proton-nucleus scattering, Phys. Rep. **212**, 223 (1992).

[17] F. J. Aguayo and H. F. Arellano, Surface-peaked medium effects in the interaction of nucleons with finite nuclei, Phys. Rev. C **78**, 014608 (2008).

[18] H. F. Arellano and J.-P. Delaroche, Low-density homogeneous symmetric nuclear matter: Disclosing dinucleons in coexisting phases, Eur. Phys. J. A **51**, 7 (2015).

[19] H. F. Arellano, F. A. Brieva, and W. G. Love, Role of nuclear densities in nucleon elastic scattering, Phys. Rev. C **42**, 652 (1990).

[20] J. W. Negele, Structure of finite nuclei in the local-density approximation, Phys. Rev. C **1**, 1260 (1970).

[21] H. F. Arellano and G. Blanchon, SWANLOP: Scattering waves off nonlocal optical potentials in the presence of Coulomb interactions, Comput. Phys. Commun. **259**, 107543 (2021).

[22] H. F. Arellano and G. Blanchon, Exact scattering waves off nonlocal potentials under Coulomb interaction within Schrödinger's integro-differential equation, Phys. Lett. B **789**, 256 (2019).

[23] L. N. Blumberg, E. E. Gross, A. Van der Woude, A. Zucker, and R. H. Bassel, Polarizations and differential cross sections for the elastic scattering of 40-MeV protons from ^{12}C, ^{40}Ca, ^{58}Ni, ^{90}Zr, and ^{208}Pb, Phys. Rev. **147**, 812 (1966).

[24] A. Nadasen, P. Schwandt, P. P. Singh, W. W. Jacobs, A. D. Bacher, P. T. Debevec, M. D. Kaitchuck, and J. T. Meek, Elastic scattering of 80–180 MeV protons and the proton-nucleus optical potential, Phys. Rev. C **23**, 1023 (1981).

[25] H. Seifert, J. J. Kelly, A. E. Feldman, B. S. Flanders, M. A. Khandaker, Q. Chen, A. D. Bacher, G. P. A. Berg, E. J. Stephenson, P. Karen, B. E. Norum, P. Welch, and A. Scott, Effective interaction for $^{16}\mathrm{O}(\mathrm{p},\mathrm{p}')$ and $^{40}\mathrm{Ca}(\mathrm{p},\mathrm{p}')$ at $E_p =$ 200 MeV, Phys. Rev. C **47**, 1615 (1993).

[26] D. A. Hutcheon, W. C. Olsen, H. S. Sherif, R. Dymarz, J. M. Cameron, J. Johansson, P. Kitching, P. R. Liljestrand, W. J. McDonald, C. A. Miller, G. C. Neilson, D. M. Sheppard, D. K. McDaniels, J. R. Tinsley, P. Schwandt, L. W. Swenson, and C. E. Stronach, The elastic scattering of intermediate energy protons from ^{40}Ca and ^{208}Pb, Nucl. Phys. A **483**, 429 (1988).

[27] D. R. Entem and R. Machleidt, Accurate charge-dependent nucleon-nucleon potential at fourth order of chiral perturbation theory, Phys. Rev. C **68**, 041001(R) (2003).

[28] G. Blanchon and H. F. Arellano, Microscopic bell-shape nonlocality: the case of proton scattering off ^{40}Ca at 200 MeV, arXiv:2402.15009.

[29] K. M. Watson, Multiple scattering and the many-body problem—Applications to photomeson production in complex nuclei, Phys. Rev. **89**, 575 (1953).

[30] A. K. Kerman, H. McManus, and R. M. Thaler, The scattering of fast nucleons from nuclei, Ann. Phys. **8**, 551 (1959).
[31] H. F. Arellano, F. A. Brieva, and W. G. Love, Full-folding-model description of elastic scattering at intermediate energies, Phys. Rev. Lett. **63**, 605 (1989).
[32] C. R. Chinn, Ch. Elster, R. M. Thaler, and S. P. Weppner, Propagator modifications in elastic nucleon-nucleus scattering within the spectator expansion, Phys. Rev. C **52**, 1992 (1995).
[33] H. F. Arellano and E. Bauge, Functional medium dependence of the nonrelativistic optical model potential, Phys. Rev. C **76**, 014613 (2007).